Journal of Materials Chemistry A

PAPER

View Article Online
View Journal | View Issue

Cite this: J. Mater. Chem. A, 2014, 2, 15509

Surface properties of α-MnO_2: relevance to catalytic and supercapacitor behaviour†

David A. Tompsett,* Stephen C. Parker and M. Saiful Islam*

Received 24th February 2014
Accepted 25th July 2014

DOI: 10.1039/c4ta00952e

www.rsc.org/MaterialsA

Hollandite (α-)MnO_2 gives superior performance compared to other MnO_2 polymorphs in surface sensitive applications in supercapacitors and catalysis. However, a thorough understanding of its atomic-scale surface properties is lacking, which we address here using density functional theory (DFT). A Wulff construction based upon relaxed surface energies demonstrates that the equilibrium morphology expresses the low index (100), (110) and (111) surfaces as well as the high index (211) and (112) surfaces. The predicted morphology exhibits clear elongation along the *c*-axis which is consistent with the large number of nanorod type structures that are obtainable experimentally. The surface structures expressed in the morphology are discussed in detail and it is found that α-MnO_2 gives rise to larger surface relaxations than are observed for the less open rutile structured MnO_2. Enhanced magnetic moments at surface sites are rationalised by a crystal field argument. Experimental studies consistently find that α-MnO_2 has higher catalytic activity than other polymorphs of MnO_2. In this work, calculated formation energies for oxygen vacancy defects at the expressed surfaces are demonstrably lower, by ~1 eV, than for rutile MnO_2 surfaces [Tompsett *et al.*, *JACS*, 2014, **136**, 1418]. The lowest vacancy formation energy occurs at the (112) surface, which despite its relative high Miller index constitutes 17% of the surface area of the calculated morphology. This may play a key role in the favourable catalytic performance observed for α-MnO_2 in a broad range of applications.

1 Introduction

Energy storage technologies for electric vehicles and grid storage of renewable energy are major research activities for which the Li–O_2 battery and supercapacitors are key candidate systems. Rising demand is driving research into new materials to provide the energy storage capabilities for a low-carbon future.[1]

While the conventional Li-ion rechargeable battery based upon a layered $LiCoO_2$ intercalation cathode has been a stalwart of the portable electronics market, future applications will require even higher energy storage densities.[2] Consequently, the high capacity Li–O_2 battery is the subject of intensive research for which α-MnO_2 is a promising catalyst.[3] Furthermore, α-MnO_2 has been demonstrated to deliver high capacitance as a supercapacitor electrode, particularly in nanostructured form.[4,5] In both technologies the good performance is directly connected to the surface properties of α-MnO_2, but despite this the structures and defect formation remain poorly characterised. With a clear motivation to better understand the performance of this material in catalytic and supercapacitor applications, in this work we apply density functional theory (DFT) simulations to understand surface phenomena in this promising material.

Experimental studies have demonstrated that α-MnO_2 is capable of being synthesised in a diverse array of nanostructures.[3,6–10] Since the material surface area is critical to electrochemical capacitance, investigators have exploited nanostructuring to obtain dramatically improved storage in supercapacitors based on α-MnO_2. Recent studies[4,5,11] of nanostructured α-MnO_2 have demonstrated capacitances as high as 328 F g^{-1}.

α-MnO_2 has also shown promise as a catalyst for the oxygen reduction reaction (ORR).[3,12,13] Historically, materials containing precious metals such as platinum, palladium and gold have been the most successful catalysts for the ORR. However, the high cost and limited availability of these materials is prohibitive in important commercial applications. In the search for a low cost alternative, manganese oxides have drawn particular attention due to their elemental abundance, high activity in alkaline media and non-toxicity.[14–19] While there are many polymorphs of MnO_2, α-MnO_2 in particular has demonstrated high catalytic activity with respect to other polymorphs[20–22] beyond the effects of high surface area.[12]

The Li–O_2 battery is an alternative to Li-ion batteries that is the subject of intense interest due to its high theoretical energy density.[1,3,23–27] However, experimental studies have shown that

Department of Chemistry, University of Bath, Bath BA2 7AY, UK. E-mail: dt331@bath.ac.uk; m.s.islam@bath.ac.uk; Fax: +44 (0)1225 386231; Tel: +44 (0)1225 384938

† Electronic supplementary information (ESI) available. See DOI: 10.1039/c4ta00952e

present implementations of the Li–O_2 system may suffer from poor electrical efficiency, in particular due to overpotentials, and power density limitations.[26,28] To address these issues the use of transition metal oxide catalysts has been suggested,[29,30] and nanorod α-MnO_2 demonstrated effective catalytic activity for this purpose.[3,31–36] However, recently the detection of electrolyte decomposisition[8,12,37,38] in Li–O_2 cells has highlighted the need to explore the performance of catalysts in stable electrolyte conditions. With recent demonstrations of good electrolyte stability during cycling of redesigned Li–O_2 cells[27,39,40] it is likely that the utility of catalysts will be important to future studies.

In other work, α-MnO_2 has exhibited good catalytic activity in applications beyond Li–O_2 cells, including the reduction of NO_x,[41] microbial fuel cells,[42] oxidation of chlorobenzene,[43] phenol degradation,[44,45] toluene oxidation[46,47] as well as oxidation of CO and benzene.[48]

Fig. 1 shows the unit cell of α-MnO_2 where the approximate MnO_6 octahedra are indicated by polyhedra. In-plane there are both corner and edge sharing octahedra forming a 2 × 2 tunnel structure along the *c*-axis. Along the *c*-axis all of the octahedra are edge sharing forming a densely packed wall to the tunnel. The 2 × 2 tunnel structure has been described as "open" compared to the comparatively denser rutile (β) polymorph of MnO_2 and this has been implicated in its excellent catalytic performance.[21] The rationalisation is based upon the reduced structural disortion and bond-breaking that is required in important catalytic processes such as oxygen defect formation and adsorption. The large 2 × 2 tunnels also provide insertion channels for adsorbed ions such as Li-ions when α-MnO_2 is used as a battery intercalation cathode.[49] Indeed, a previous modelling study of α-MnO_2 by Trahey *et al.*[50] has treated the thermodynamics of Li-ion and Li-oxide insertion at the surface of α-MnO_2. Based upon the obtained insertion potentials they suggested that Li-oxide insertion and extraction may be an active mechanism in the performance of α-MnO_2 as a catalyst in the Li–O_2 battery system.

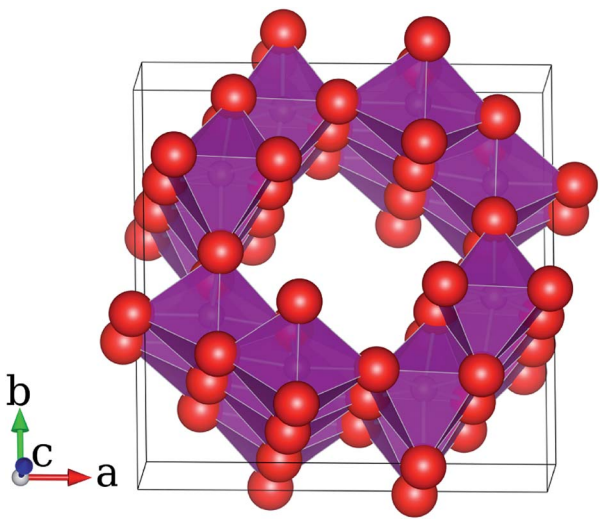

Fig. 1 Crystal structure of α-MnO_2. Small (red) spheres are oxygen and large (purple) manganese lie inside the indicated approximate MnO_6 octahedra. Note the large 2 × 2 tunnel structures along the *c*-axis.

A recent DFT study by Ling and Mizuno[51] has considered Li-ion and Li-oxide insertion into bulk α-MnO_2. That work considered structural distortions upon lithiation and the thermodynamics of insertion. They also considered the effect of Li_2O insertion upon the electronic structure. Li and Na insertion into bulk α-MnO_2 has been considered by some of the present authors using DFT.[52] Cockayne and Li[53] have studied the magnetic structure and the adsorption of dopants for bulk α-MnO_2 and Crespo *et al.* also treated the magnetic structure using DFT.[54] Liu *et al.* recently considered the surface energy and magnetic order of the (110) surface of α-MnO_2 by similar methods.[55] Cheng *et al.* used DFT to consider adsorption of oxides at rutile MnO_2 surfaces.[56] They found that oxygen vacancies enhance the interaction between oxide species and the MnO_2 surface. Furthermore, the presence of oxygen vacancies reduced the enthalpy of the oxygen reduction process at MnO_2 surfaces by more than 2 eV. A recent first-principles study of manganese oxides catalysts for the ORR and oxygen evolution reaction (OER) constructed Pourbaix diagrams of stable surface configurations of MnO_x stoichiometries as a function of applied potential and pH.[57] That work found that the oxygen adsorbed (110) surface of rutile MnO_2 was active at experimental conditions for the OER. However, as highlighted by the authors they did not consider the presence of α-MnO_2, nor the energetics of oxygen vacancy formation.

Due to the renewed interest in α-MnO_2, in this work we perform a comprehensive *ab initio* study of its surface properties. The study of α-MnO_2 surfaces in the present work shows a tendency for this material to form rod-like morphologies that are elongated along the *c*-axis, which is likely to be important to the formation of nanostructures with improved capacitance. First we outline our computational methods. Then we present results on the structures and energies of stoichiometric surfaces, as well as the equilibrium crystal morphology. Following this the calculated energetics of oxygen vacancy formation at surfaces are discussed with reference to catalytic activity.

2 Computational methods

Ab initio simulations of surface energies and morphologies, particularly in complex and lower symmetry structures, are computationally expensive. In this study, we aim to take advantage of efficient interatomic potentials as a screening tool for candidate low energy surfaces. These low energy candidates are then treated by *ab initio* DFT which more fully describes the electronic effects in the system.

This study employs well-established interatomic potentials methods, which are reviewed in detail elsewhere.[58–60] The model due to Parker and co-workers[61,62] for rutile β-MnO_2, that has been utilised successfully in several studies,[63,64] is augmented by the inclusion of a core–shell model for the oxygen. The model reproduces the experimental lattice parameters of α-MnO_2 within 1.5% and full details are presented in the ESI.† The interactions between ions are represented in terms of a long-

range coulombic term with the addition of an analytic term representing short-range interactions. The surface energies from interatomic potentials were then calculated using the METADISE code[65] up to high indexes.

Candidate low energy surfaces obtained from interatomic potentials were then treated by DFT as implemented in the VASP code[66] with PAW potentials. The electronic structure was calculated using the Generalized Gradient Approximation (GGA) of Perdew, Burke and Ernzerhof[67] with Hubbard U corrections (PBE + U). The PBE + U exchange–correlation functional has been demonstrated to give a good description of defect properties in other oxides including CeO_2 (ref. 68) and TiO_2.[69] All calculations were performed in a ferromagnetic spin polarised configuration, while effects of more complex magnetic order, due to their low energy scale, are left for future work. To obtain the equilibrium lattice parameters by relaxation of the bulk cell a cutoff for the planewave basis set of 520 eV was used to avoid Pulay stress. All subsequent calculations were performed based upon the obtained equilibrium lattice constants without cell relaxation using a cutoff of 400 eV. This included the recalculation of the energy for the bulk unit cell so that all comparative energies were obtained at a constant cutoff of 400 eV. A minimum of $4 \times 4 \times 4$ k-points was used in the Brillouin zone of the conventional cell and scaled appropriately for supercells.

The value of the U parameter for our PBE + U calculations was determined *ab initio* using Wien2k.[70,71] Previous work conducted by some of the present authors[72,73] demonstrated a good description of lithium intercalation, band gaps and magnetic interactions when PBE + U is applied in the fully-localized limit,[74] which we use in this work as well. We employ $(U - J) =$ 5.2 eV, for the spherical part of the interaction, and $J = 1.0$ eV. Further details are described in the ESI.† These parameters have been shown to give accurate results for the thermodynamics of Li-ion insertion and electronic structure of α-MnO_2 in previous work by some of the present authors.[52]

The α-MnO_2 crystal occurs in the tetragonal space group $I4/m$ (# 87) with lattice parameters[75] $a = b = 9.750$ Å and $c = 2.861$ Å. In Table 1 we show the calculated lattice parameters for α-MnO_2 from PBE + U. These results agree with the experimental parameters within 2.5%, but the common tendency for PBE + U to overestimate the unit cell volume is evident.[76]

Surface energies are calculated based upon slabs with a minimum thickness of 20 Å, where for each surface the slab thickness is increased until convergence of the surface energy is obtained. A vacuum thickness greater than 20 Å was used throughout to separate the slabs from their periodic image. All dipole free surface terminations were considered with Miller indices up to and including 2. Full geometrical relaxation of the ionic positions until the forces fell below 0.02 eV $Å^{-2}$ was performed to incorporate surface relaxation effects.

To obtain the defect energies with respect to the stoichiometric surface, a single k-point PBE calculation of an isolated spin triplet oxygen molecule in a 15 Å side cubic cell was performed using the same energy cutoff and convergence criterion as for the slab calculations. From this we obtain a reference energy of −9.85 eV for the oxygen molecule. However, the PBE + U functional is known to give rise to errors in formation energies of oxide materials due to both an inadequate description of the oxygen molecule (including overbinding) and of the solid oxides. Hence as in previous work,[77] to obtain an estimate of the error relevant to the process of oxygen vacancy formation with accompanying Mn reduction at α-MnO_2 surfaces we have calculated the enthalpy of the following reaction:

$$MnO_2 \rightarrow \frac{1}{2}Mn_2O_3 + \frac{1}{4}O_2 \quad (1)$$

This reaction incorporates the removal of oxygen and the reduction of Mn. Comparison of the reaction enthalpy from our PBE + U calculation with the experimental enthalpy (40.5 kJ mol^{-1})[78] indicates a correction of 1.07 eV per oxygen. The correction is applied to all oxygen vacancy formation energies quoted in this work.

Table 1 Predicted PBE + U and experimental[75] lattice parameters for α-MnO_2

α-MnO_2	a (Å)	b (Å)	c (Å)
PBE + U	9.907	9.907	2.927
Experimental	9.750	9.750	2.861

3 Surface energies and crystal morphology

Experimentally, α-MnO_2 has been synthesised in a range of morphologies. Commonly, the synthesised material resembles a network of small nanorods at the nanoscale.[10,79] However, computational studies of the surfaces expressed in these crystals are lacking. Before a good understanding of the catalytic and surface properties in this system can be obtained it is essential that the characteristics of the exposed surfaces are understood at the atomic-scale. In this section we address these issues by the calculation of surface energies from which we determine a Wulff constructed crystal morphology.

First-principles surface studies deliver high accuracy, but are computationally costly. Consequently, practitioners are generally forced to treat only a limited set of surfaces, while experimentally the number of possible combinations of Miller indexes is notionally infinite. Typically, low index surfaces, *i.e.* those with only 1's and 0's like (110), are chosen for this set due to their tendency to have favourable surface coordination. In this work favourable coordinations are those close to the 6-fold Mn–O coordination found in the bulk of MnO_2. However, our recent study[77] of rutile MnO_2 surfaces has demonstrated that relatively high coordination and low surface energy does occur for high Miller indexes. To screen high Miller index surfaces we have calculated the surface energies of 34 surfaces with our interatomic potentials model. The resulting surface energies are shown in ESI Table S2 and the resulting Wulff constructed morphology in Fig. S1.† We have then treated all low index surfaces, and high index surfaces that are low in energy, by first-principles PBE + U.

Table 2 Predicted PBE + U surface energies for α-MnO_2

Miller index	E_{surf} (J m^{-2})
(100)	0.64
(001)	1.76
(110)	0.75
(111)	1.32
(101)	1.91
(102)	1.55
(112)	1.40
(122)	1.54
(201)	1.51
(211)	1.08
(221)	1.59
(310)	1.41

In Table 2 we show the obtained PBE + U surface energies for α-MnO_2. The surface energy is calculated by taking the difference between the energy of the constructed slab and the same number of α-MnO_2 formula units in the bulk:

$$\gamma = \frac{E_s - nE_b}{2A} \quad (2)$$

where, E_s is the energy of a slab containing n formula units and E_b is the total energy per formula unit of bulk α-MnO_2. A is the area of the slab surface and the factor of 2 reflects the fact that there are two surfaces for each slab. The (100) and (110) surfaces, with low energies of 0.64 and 0.75 J m^{-2} respectively, are the most stable. All other surface energies are greater than 1 J m^{-2}.

We will return to discuss the surface terminations and electronic properties in more detail, but first we present the morphology of α-MnO_2 from a Wulff construction using these energies. The resulting morphology is shown in Fig. 2 and has an elongated shape, which is consistent with the large number of experimental synthesis studies that observe nanorod crystals.[3,8,79–83] The (100) surface dominates and represents 54% of the crystal surface area followed by the (110) surface that is 20% of the surface area. However, the high index (112) surface represents a substantial 17% of the area.

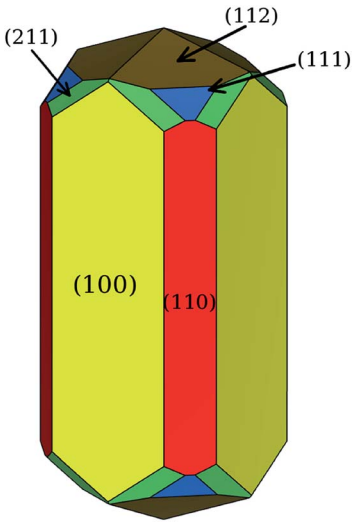

Fig. 2 The predicted equilibrium crystal morphology for α-MnO_2 based upon the surface energies in Table 2.

The presence of the (100) surface has been observed by Transmission Electron Microscopy (TEM) experiments of Zhang *et al.*[79] based upon measured fringe spacings of α-MnO_2 nanorods. Furthermore, TEM studies have indicated the presence of the (110) surface[8,80,81] in synthesized nanostructured α-MnO_2. These observations are consistent with the calculated low energy for these surfaces and their expression in the Wulff morphology of Fig. 2. These results indicate that the calculated surface energies are consistent with observed experimental morphologies. To our knowledge the present work is the first comprehensive study of the morphology of α-MnO_2 and the good correspondence with experiment shows the ability of computational simulations to enhance our understanding of this system.

Finally, some experimental studies also suggest the presence of the (310) surface,[82,83] where we note the reaction of permanganate MnO_4^- with acidic reagents, H_2SO_4 and HNO_3, in both of those studies. However, our calculated surface energy of 1.41 J m^{-2} for the (310) surface indicates that its expression is likely to be a result of non-equilibrium synthesis conditions. A treatment of off-stoichiometry at α-MnO_2, such as was recently performed by Oxford *et al.*[84] for low index surfaces of rutile MnO_2, may allow further insight regarding the morphological dependence upon experimental synthesis conditions. Such investigations, which like the present study require a large computational cost, will be the subject of future work.

4 Surface structures and magnetic moments

In order to fully understand the impact of the surfaces of α-MnO_2 on its catalytic and electrochemical performance it is essential to probe these surfaces beyond the calculation of their energies. Having determined the surface energies and resulting Wulff crystal morphology, in this section we inspect the atomic structure at specific cleaved surfaces in detail. The goal here is to understand how the fundamental characteristics of the cleaved crystal drive the creation of the obtained elongated morphology and furthermore to gain insight into the phenomenology that occurs at these surfaces when α-MnO_2 is used in electrochemical and catalytic applications.

In Table 3 we summarize the coordination numbers and magnetic moments for the surface Mn ions of the low energy surfaces. We begin by considering the (100) surface that dominates the Wulff morphology. The (100) surface Mn ions are clearly well coordinated with three of the four surface sites possessing 6-fold Mn–O coordination. Indeed 6-fold coordination is the same as that which occurs in the octahedra that are the building block of the bulk α-MnO_2 crystal. The fact that the cleavage plane that forms the (100) surface, shown in Fig. 3, maintains the 6-fold coordination so well is very likely to be important to the low calculated surface energy of 0.64 J m^{-2}.

Table 3 Mn–O coordinations and magnetic moments for low energy surfaces of α-MnO_2. Surface Mn-ions are labeled as in Fig. 3–7

Surface	Site	n_{coord}	Moment (μ_B)
(100)	Mn(1)	5	3.70
	Mn(2)	6	3.12
	Mn(3)	6	3.12
	Mn(4)	6	3.15
(110)	Mn(1)	5	3.55
	Mn(2)	6	3.17
	Mn(3)	6	3.12
(111)	Mn(1)	3	4.31
	Mn(2)	4	3.88
	Mn(3)	4	3.43
	Mn(4)	5	3.35
	Mn(5)	5	3.28
(211)	Mn(1)	5	2.99
	Mn(2)	5	2.91
	Mn(3)	5	3.14
	Mn(4)	4	1.83
(112)	Mn(1)	3	3.87
	Mn(2)	4	3.80
	Mn(3)	4	3.97
	Mn(4)	5	3.43

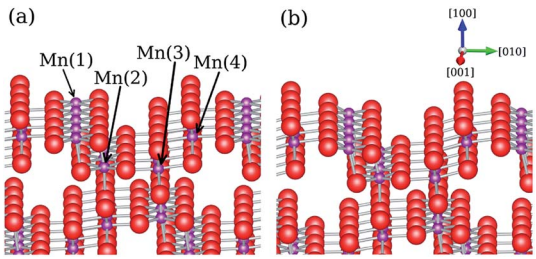

Fig. 3 Structure of the (100) surface of α-MnO_2: (a) before relaxation and (b) after relaxation.

The stability of the cleaved surface is also evident in a comparison of the surface before relaxation (Fig. 3(a)) and after relaxation (Fig. 3(b)). The primary difference between the structures is a small outwards movement of two oxygen ions that coordinate Mn(1). This outward movement acts to improve the coordination sphere around Mn(1) which is the only 5-fold site produced by the (100) cleavage plane. Oxygen terminated surfaces may present favoured sites for ion adsorption, *e.g.* H^+, when α-MnO_2 is employed as a supercapacitor electrode. Finally, as shown in Table 3 there is a clear enhancement of the magnetic moment for Mn(1) to 3.70 μ_B due to its lower 5-fold coordination, while the 6-fold coordinate Mn(2–4) possess bulk-like moments of ~3.12 μ_B. This indicates that structural surface distortions do have a marked effect on the electronic properties and we will return to discuss the causes of this enhancement in detail.

At the (110) surface the coordination of Mn ions, listed in Table 3, is high, two Mn ions being 6-fold and one 5-fold coordinate. This is a significant contributor to the low surface energy of 0.75 J m^{-2} obtained at this surface. As shown in Fig. 4 this surface has the structure of a series of repeating ledges

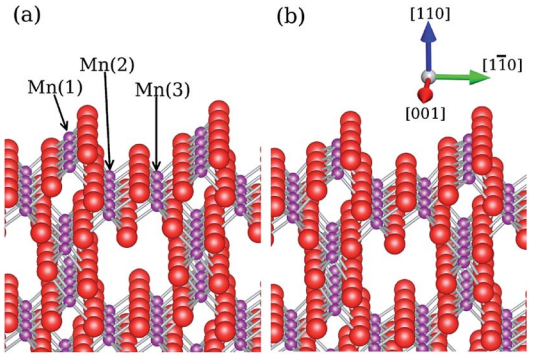

Fig. 4 Structure of the (110) surface of α-MnO_2: (a) before relaxation and (b) after relaxation.

formed by rows of oxygen ions that run along the [001] direction. Prominent at the surface is a bridging oxygen ion attached to Mn(1) ions. Indeed it is the relaxation of this oxygen site that dominates the structural relaxation at the cleaved surface. However, due to the good coordination at this surface, average coordination number $5\frac{2}{3}$, the crystal structure undergoes only a small amount of relaxation when cleaved as indicated by a comparison of Fig. 4(a) and (b). Furthermore, since the bridging oxygen site is only attached to two Mn ions it is likely to be a site of facile oxygen vacancy formation, which is relevant to the catalytic activity of α-MnO_2. The (110) surface was also found to be expressed in a Wulff morphology of rutile MnO_2 (ref. 62) and together with the (100) dominates the make up of the in-plane components of the calculated equilibrium morphology in α-MnO_2.

The crystal morphology must be capped by surfaces with a Miller index that includes a non-zero *c*-axis component. The (111) facet with a surface energy of 1.32 J m^{-2} forms part of the end cap for the calculated morphology in Fig. 2, but is significantly higher in energy than the (110) and (100) surfaces. The end cap of the morphology refers to facets that have some component of their surface normal along the *c*-axis *i.e.* they form part of the ends of the rod. It is the disparity in energy between the lower energy in-plane (110) and (100) surfaces, and the higher energy surfaces that cap the morphology that leads to

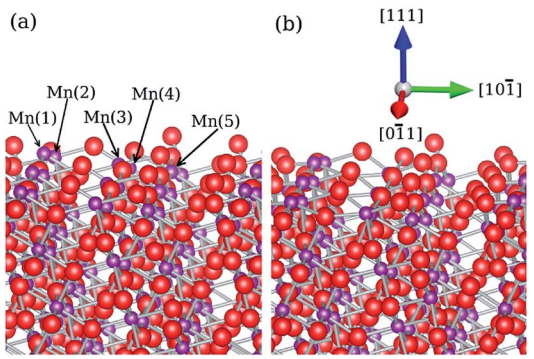

Fig. 5 Structure of the (111) surface of α-MnO_2: (a) before relaxation and (b) after relaxation.

its elongated structure. The qualitative reason for the disparity in surface energies may be ascertained from Table 3 where it is clear that the Mn ions at the (110) and (100) surfaces possess higher coordination than at any other expressed surface. Inspection of Fig. 5 shows that the (111) surface has a complex structure with five symmetry inequivalent surface Mn ion sites. As listed in Table 3 the undercoordinated 3-fold Mn(1) site possesses a strongly enhanced magnetic moment of 4.31 μ_B, a topic that we will return to discuss in detail.

The (211) surface, which has a surface energy of 1.08 J m^{-2}, is also expressed in the end caps of the morphology. The average coordination number of the Mn ions at this surface, 4.75, is considerably lower than for the in-plane (100) and (110) surfaces. However, if we compare this value to the other expressed surfaces that cap the morphology their average coordination numbers are 4.2 for (111) and 4 for (112), which emphasises why the (211) is lower in energy than these surfaces. The primary relaxation at this surface, shown in Fig. 6, is the outward movement of a dangling oxygen ion that is singly bonded to the Mn(2) site. Finally, an interesting feature of the low coordinated Mn(4) ion is its low magnetic moment of just 1.83 μ_B.

The remaining surface that is expressed in the morphology is the (112) facet, which dominates the end cap surface area and represents 17% of the crystal surface area as a whole. Comparison of Fig. 7(a) and (b) indicates that the primary relaxation at the cleaved surface is the outward movement of oxygen sites to improve the coordination spheres around Mn(1) and Mn(2), which are only 3-fold and 4-fold coordinated to bonded oxygen sites. This is accompanied by a drawing in of the Mn(1) and Mn(2) sites towards the surface. We note that this indicates, along with the other expressed surfaces, a tendency to favour oxygen termination in the outermost surface layer. The presence of these oxygens may provide key sites for surface reduction during catalytic activity and cation adsorption during electrochemical application.

Finally, we return to discuss the interesting enhanced magnetic moments observed at some surface Mn sites. The presence of enhanced moments accompanies under-coordination of the surface Mn site. For instance, the 5-fold coordinated Mn(1) site of the (100) surface possesses a magnetic

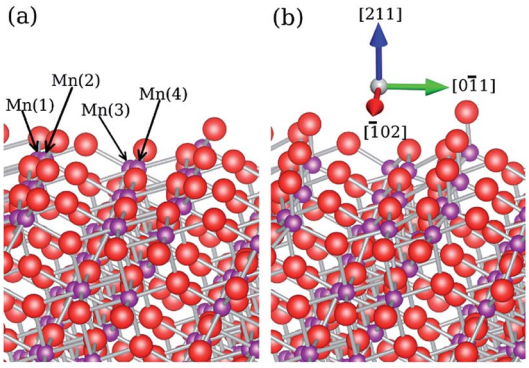

Fig. 6 Structure of the (211) surface of α-MnO_2: (a) before relaxation and (b) after relaxation.

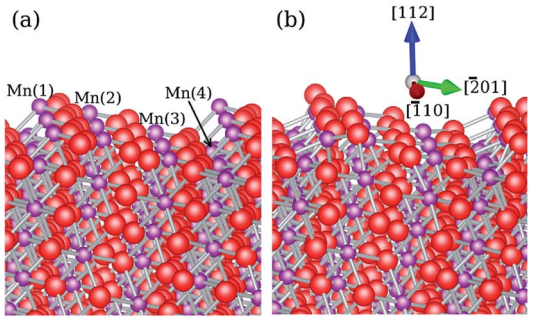

Fig. 7 Structure of the (112) surface of α-MnO_2: (a) before relaxation and (b) after relaxation.

moment of 3.70 μ_B compared to 3.10 μ_B for the bulk material. Inspection of Table 3 indicates the prevalence of these enhanced moments, which occur at all of the expressed surfaces in the crystal morphology. The enhancement of these moments strongly suggests a tendency for the presence of Mn^{3+} (d^4) at the surfaces, as demonstrated by a recent X-ray photoelectron spectroscopy study of α-MnO_2 nanowires.[34] This is consistent with the absence of a full coordination sphere of electronegative O ions around these sites. However, we emphasise that our calculations indicate that α-MnO_2 should not be thought of as purely ionic but possesses intermediate ionic-covalent character.

At the (111) surface the low 4-fold coordination of the Mn(2) site results in an enhancement of the magnetic moment to 3.88 μ_B. However, there is no clear mathematical relationship between coordination number and magnetic moment. Rather, the resulting magnetic moment depends not only on the coordination number, but also the specific geometry of the coordination. For the Mn(2) 4-fold coordinate sites at the (111) and (112) surfaces the Mn environment can best be thought of as severed octahedral. Compared to an octahedral environment the Mn coordination is missing a bond along the x and y directions, which lowers the energy of the d_{xy} and $d_{x^2-y^2}$ orbitals as shown in Fig. 8(a). It is clear that the moment of 3.88 μ_B at the (111) surface corresponds to a high spin state. Enhanced moments in this environment have recently been observed in a combined experimental (NMR and magnetic susceptibility) and theoretical investigation of Co sites in $LiCoO_2$.[85] For (211) the 4-fold coordinate environment is more like a strongly distorted tetrahedral environment as depicted in Fig. 8(b), which results in a low spin moment of 1.80 μ_B. In the perfect tetrahedral

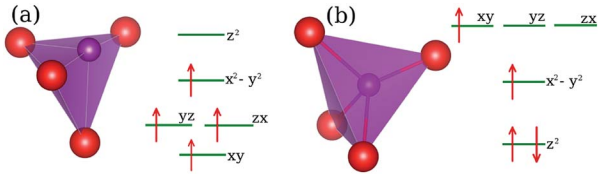

Fig. 8 Structure of the crystal field environment for (a) the high spin 4-fold Mn(2) sites at the (111) surface and (b) the low spin 4-fold Mn(4) site at the (211) surface.

environment the e_g orbital lies lower than the t_{2g}. However, the distorted tetrahedron possesses one bond angle that is strongly decreased from the ideal 109.5° to 87°. Furthermore, one of the Mn–O bond lengths is contracted to 1.59 Å. These distortions split the e_g orbital by increasing the $d_{x^2-y^2}$ energy. This results in the 4-fold Mn site of the (211) surface possessing a double occupation of the d_{z^2} orbital and a low spin moment. Further analysis of the unusual surface electronic structure is warranted, but since our prime motivation is to explore surface morphologies and oxygen vacancy formation this will be pursued in future work.

5 Oxygen vacancy formation and catalytic activity

α-MnO_2 has been demonstrated to have high catalytic activity. A recent study by Giordani *et al.* showed that α-MnO_2 delivered the highest catalytic activity for the decomposition of H_2O_2 when tested alongside a set of other transition metal oxides.[86] Furthermore, comparative investigations[3,21,87] consistently indicate that the hollandite crystal structure of α-MnO_2 delivers substantially better catalytic performance than other polymorphs of MnO_2. Consequently, a key question for this section is to answer why studies persistently find the α polymorph to have the highest catalytic activity.

The process of oxygen defect formation at MnO_2 surfaces may play a key role in its catalytic activity. For instance, the Mars-van Krevelen mechanism[88] requires a redox process in which oxygen is consumed from the surface and then replenished from the gas phase. Recent work has shown that the presence of oxygen vacancies at rutile MnO_2 surfaces enhances its catalytic activity for the ORR,[41,56,89] which makes this investigation of surface properties timely. Indeed an *in situ* X-ray photoelectron study of the catalytic activity of α-MnO_2 for reduction of NO and N_2O correlated high catalytic performance with the presence of Mn^{3+} ions and oxygen vacancies.[41] Vacancy formation energies have been calculated according to the following reduction process:

$$O_O^{\times} + 2Mn_{Mn}^{\times} \rightarrow V_O^{\cdot\cdot} + 2Mn_{Mn}^{\prime} + \frac{1}{2}O_{2(g)} \quad (3)$$

where Kroger-Vink notation has been used. Here, the lattice site that a species occupies is indicated by the subscript, and the superscript shows the electric charge of the species relative to that of the charge of that site in a stoichiometric crystal: × indicates no change to the charge, a single ′ represents a negative charge and a · represents a positive charge. We note that this process incorporates oxygen vacancy formation as well as the reduction of Mn^{4+} to Mn^{3+}, which corresponds to the process observed by X-ray photoelectron experiments.[41]

The defect energies for removal of all symmetry inequivalent surface oxygens have been calculated and the lowest defect energy obtained for each surface is shown in Table 4. Since it is the dilute, low concentration vacancy defects that are likely to be important to catalysis the defect formation energies were calculated for large surface supercells and converged with respect to slab thickness.

Table 4 Predicted PBE + *U* oxygen vacancy formation energies at surfaces of α-MnO_2 based on eqn (3)

Miller index	ΔE_f (O-vac) (eV)
(100)	1.02
(110)	0.97
(111)	0.30
(211)	1.09
(112)	0.07
Bulk	2.57

The key results firstly, reveal the low defect formation energies of 0.07 eV and 0.3 eV for the (112) and (111) surfaces respectively. Secondly, there are low defect formation energies at all expressed surfaces. In fact, the *highest* energy of 1.09 eV at the (211) surface is only slightly higher than the *lowest* defect formation energy of 0.96 eV obtained for rutile MnO_2 surfaces in a recent study by the present authors.[77] This strongly suggests that the good catalytic performance of α-MnO_2 compared to other transition metal oxides and other polymorphs of MnO_2 results from the facile oxygen vacancy formation at its surfaces.

It is worth noting that surface coordination, which we have discussed for its impact on surface energies and magnetic moments, is also important to the energetics of oxygen vacancy formation. For example, to provide the low formation energy of 0.07 eV at the (112) surface an oxygen that is attached to the 5-fold coordinate Mn(4) site is removed. For the low formation energy of 0.3 eV at the (111) surface an oxygen is removed at a 6-fold site in the subsurface. However, we note that it is not only the coordination of manganese sites that is important, but also the Mn coordination around the removed oxygen. For example, at the (110) surface the removal of a bridging oxygen from the 5-fold coordinate Mn(1) is favoured over the removal of oxygens that are attached to 6-fold Mn(2) sites because such oxygens give coordination to three manganese sites, while removing the bridging oxygen only breaks the coordination of two Mn sites. Therefore, we suggest empirically that oxygen vacancy formation is most favourable when the removed oxygen has low coordination to Mn, but the attached Mn sites have high coordination to oxygen.

It is interesting to note that the bulk oxygen vacancy defect formation energy of 2.57 eV is actually slightly higher than that calculated for bulk rutile MnO_2 (2.26 eV). Consequently, it is clear that the surfaces produced by cleaving the α-MnO_2 crystal structure are the important factor in the facile production of oxygen vacancies, rather than its bulk properties.

The crystal structure of α-MnO_2 is more open than other polymorphs such as rutile and ramsdellite due to the presence of the large 2 × 2 tunnel structures. The importance of this openness has been discussed with reference to the high catalytic activity of α-MnO_2 for oxidation of CO.[21] Upon cleaving, the more open crystal structure gives rise to a greater diversity of oxygen surface sites as well as better overall coordination of Mn surface sites compared to rutile MnO_2. While effects of the

electronic structure will also be important, this larger phase space in the surface crystal structure is likely to be a key influence on the low oxygen vacancy formation energies.

The low defect formation energies obtained at α-MnO_2 surfaces demonstrate a mechanism for its good catalytic performance for the ORR. The results clearly indicate that the catalytic activity is driven by fundamental surface properties, beyond the large surface area of nanoparticles. These high performance properties make it an important, low cost alternative to precious metal catalysts for technological applications, including the topical Li–O_2 battery.

6 Conclusions

Advanced materials simulations have been employed to enhance our understanding of α-MnO_2 surfaces, an important material for technological applications. The key findings include:

(1) The calculated equilibrium morphology is elongated along the *c*-axis, which is consistent with the large number of nanorod structures obtained from experimental synthesis. The (100) and (110) surfaces dominate the in-plane morphology and constitute 54% and 20% of the overall surface area respectively. Both surfaces have been observed by TEM experiments. The surfaces that form the ends of the rod-like morphology are substantially higher in energy, by more than 45%, which is the driver of the elongation along the *c*-axis.

(2) Due to their ability to provide favourable surface coordination, the higher Miller index (211) and (112) surfaces are expressed in the morphology. Coordination at surface sites is found to be important to obtaining low surface energies. The open crystal structure of α-MnO_2 with 2×2 tunnels provides a large number of surface configurations for satisfying surface coordinations.

(3) We find evidence for the presence of both enhanced high spin and low spin Mn sites at cleaved surfaces. The magnetic moments are explained rationally by the crystal field energy scales in the cleaved surface environments.

(4) Regarding the key question as to why α-MnO_2 provides higher catalytic activity than other related oxide materials, our results present compelling evidence that facile oxygen vacancy formation is at play. The low oxygen vacancy formation energies, all in the range 0.07 eV to 1.09 eV, indicate a favourable thermodynamic pathway for catalytic processes, for instance *via* the Mars-van Krevelin mechanism. The results demonstrate that the catalytic activity of α-MnO_2 is not merely a consequence of the large surface area of synthesised nanoparticles.

Acknowledgements

We are grateful to Chris Eames for discussions, the EPSRC for funding (EP/H019596; EP/H003819) and to the Materials Chemistry Consortium (EP/L000202) for Hector supercomputer resources.

References

1 P. G. Bruce, S. A. Freunberger, L. J. Hardwick and J.-M. Tarascon, *Nat. Mater.*, 2012, **11**, 19.
2 J. B. Goodenough and Y. Kim, *Chem. Mater.*, 2010, **22**, 587.
3 A. Debart, A. J. Paterson, J. Bao and P. G. Bruce, *Angew. Chem., Int. Ed.*, 2008, **47**, 4521–4524.
4 H. Jiang, T. Sun, C. Li and J. Ma, *J. Mater. Chem.*, 2012, **22**, 2751–2756.
5 D. P. Dubal, R. Holze and P. M. Kulal, *J. Mater. Sci.*, 2013, **48**, 714–719.
6 F. Y. Cheng, J. Z. Zhao, W. Song, C. S. Li, H. Ma, J. Chen and P. W. Shen, *Inorg. Chem.*, 2006, **45**, 2038–2044.
7 W. Zhang, H. Wang, Z. Yang and F. Wang, *Colloids Surf., A*, 2007, **304**, 60.
8 M. Xu, L. Kong, W. Zhou and H. Li, *J. Phys. Chem. C*, 2007, **111**, 19141–19147.
9 S. Devaraj and N. Munichandraiah, *J. Phys. Chem. C*, 2008, **112**, 4406–4417.
10 J. Zeng, J. R. Nair, C. Francia, S. Bodoardo and N. Penazzi, *Int. J. Electrochem. Sci.*, 2013, **8**, 3912–3927.
11 A. J. Roberts and R. C. Slade, *Electrochim. Acta*, 2010, **55**, 7460.
12 W. Xiao, D. Wang and X. W. Lou, *J. Phys. Chem. C*, 2010, **114**, 1694.
13 A. K. Thapa and T. Ishihara, *J. Power Sources*, 2011, **196**, 7016.
14 V. M. B. Crisostomo, J. K. Ngala, S. Alia, A. Dobley, C. Morein, C. H. Chen, X. F. Shen and S. L. Suib, *Chem. Mater.*, 2007, **19**, 1832.
15 Z. X. Liu, Y. Xing, C. H. Chen, L. Zhao and S. L. Suib, *Chem. Mater.*, 2008, **20**, 2069.
16 Y. G. Wang, L. Cheng, F. Li, H. M. Xiong and Y. Y. Xia, *Chem. Mater.*, 2007, **19**, 2095.
17 S. Shanmugam and A. Gedanken, *J. Phys. Chem. B*, 2006, **110**, 24486.
18 K. P. Gong, P. Yu, L. Su, S. X. Xiong and L. Q. Mao, *J. Phys. Chem. C*, 2007, **111**, 1882.
19 I. Roche, E. Chainet, M. Chatenet and J. Vondrak, *J. Phys. Chem. C*, 2007, **111**, 1434.
20 F. Cheng, Y. Su, J. Liang, Z. Tao and J. Chen, *Chem. Mater.*, 2010, **22**, 898–905.
21 R. Xu, X. Wang, D. Wang, K. Zhou and Y. Li, *J. Catal.*, 2006, **237**, 426.
22 V. B. R. Boppana and F. Jiao, *Chem. Commun.*, 2011, **47**, 8973–8975.
23 J. Christensen, P. Albertus, R. S. Sanchez-Carrera, T. Lohmann, B. Kozinsky, R. Liedtke, J. Ahmed and A. Kojic, *J. Electrochem. Soc.*, 2011, **159**, R1–R30.
24 N. Garcia-Araez and P. Novak, *J. Solid State Electrochem.*, 2013, **17**, 1793–1807.
25 G. Girishkumar, B. McCloskey, A. C. Luntz, S. Swanson and W. Wilcke, *J. Phys. Chem. Lett.*, 2010, **1**, 2193–2203.
26 T. Ogasawara, A. Debart, M. Holzapfel, P. Novak and P. G. Bruce, *J. Am. Chem. Soc.*, 2006, **128**, 1390–1393.
27 M. M. O. Thotiyl, S. A. Freunberger, Z. Peng, Y. Chen, Z. Liu and P. G. Bruce, *Nat. Mater.*, 2013, **12**, 1049.

28 A. Debart, J. Bao, G. Armstrong and P. G. Bruce, *J. Power Sources*, 2007, **174**, 1177–1182.
29 Y.-C. Lu, Z. Xu, H. A. Gasteiger, S. Chen, K. Hamad-Schifferli and Y. Shao-Horn, *J. Am. Chem. Soc.*, 2010, **132**, 12170–12171.
30 B. D. McCloskey, R. Scheffler, A. Speidel, D. S. Bethune, R. M. Shelby and A. C. Luntz, *J. Am. Chem. Soc.*, 2011, **133**, 18038–18041.
31 A. K. Thapa, Y. Hidaka, H. Hagiwara, S. Ida and T. Ishihara, *J. Electrochem. Soc.*, 2011, **158**, A1483–A1489.
32 M.-S. Park, J.-H. Kim, K. J. Kim, G. Jeong and Y.-J. Kim, *J. Nanosci. Nanotechnol.*, 2013, **13**, 3611–3616.
33 Y. Qin, J. Lu, P. Du, Z. Chen, Y. Ren, T. Wu, J. T. Miller, J. Wen, D. J. Miller, Z. Zhang and K. Amine, *Energy Environ. Sci.*, 2013, **6**, 519–531.
34 K. Song, J. Jung, Y.-U. Heo, Y. C. Lee, K. Cho and Y.-M. Kang, *Phys. Chem. Chem. Phys.*, 2013, **15**, 20075–20079.
35 Y. Cao, Z. Wei, J. He, J. Zang, Q. Zhang, M. Zheng and Q. Dong, *Energy Environ. Sci.*, 2012, **5**, 9765–9768.
36 T. T. Truong, Y. Liu, Y. Ren, L. Trahey and Y. Sun, *ACS Nano*, 2012, **6**, 8067.
37 S. A. Freunberger, Y. Chen, Z. Peng, J. M. Griffin, L. J. Hardwick, F. Barde, P. Novak and P. G. Bruce, *J. Am. Chem. Soc.*, 2011, **133**, 8040–8047.
38 F. Mizuno, S. Nakanishi, Y. Kotani, S. Yokoishi and H. Iba, *Electrochemistry*, 2010, **78**, 403.
39 H.-G. Jung, J. Hassoun, J.-B. Park, Y.-K. Sun and B. Scrosati, *Nat. Chem.*, 2012, **4**, 579–585.
40 Z. Peng, S. A. Freunberger, Y. Chen and P. G. Bruce, *Science*, 2012, **337**, 563–566.
41 J. Shan, Y. Zhu, S. Zhang, T. Zhu, S. Rouvimov and F. F. Tao, *J. Phys. Chem. C*, 2013, **117**, 8329.
42 S. Khilari, S. Pandit, M. M. Ghangrekar, D. Das and D. Pradhan, *RSC Adv.*, 2013, **3**, 7902–7911.
43 J. Li, C. Song and S. Liu, *Acta Chim. Sin.*, 2012, **70**, 2347–2352.
44 H. Liang, H. Sun, A. Patel, P. Shukla, Z. H. Zhu and S. Wang, *Appl. Catal., B*, 2012, **127**, 330–335.
45 E. Saputra, S. Muhammad, H. Sun, A. Patel, P. Shukla, Z. H. Zhu and S. Wang, *Catal. Commun.*, 2012, **26**, 144–148.
46 F. Shi, F. Wang, H. Dai, J. Dai, J. Deng, Y. Liu, G. Bai, K. Ji and C. T. Au, *Appl. Catal., A*, 2012, **433–434**, 206–213.
47 F. Wang, H. Dai, J. Deng, G. Bai, K. Ji and Y. Liu, *Environ. Sci. Technol.*, 2012, **46**, 4034.
48 Q. Ye, J. Zhao, F. Huo, J. Wang, S. Cheng, T. Kang and H. Dai, *Catal. Today*, 2011, **175**, 603–609.
49 D. Su, H.-J. Ahn and G. Wang, *J. Mater. Chem. A*, 2013, **1**, 4845–4850.
50 L. Trahey, N. K. Karan, M. K. Y. Chan, J. Lu, Y. Ren, J. Greeley, M. Balasubramanian, A. K. Burrell, L. A. Curtiss and M. M. Thackeray, *Adv. Energy Mater.*, 2013, **3**, 75.
51 C. Ling and F. Mizuno, *Chem. Mater.*, 2012, **24**, 3943.
52 D. A. Tompsett and M. S. Islam, *Chem. Mater.*, 2013, **25**, 2515.
53 E. Cockayne and L. Li, *Chem. Phys. Lett.*, 2012, **544**, 53–58.
54 Y. Crespo and N. Seriani, *Phys. Rev. B: Condens. Matter Mater. Phys.*, 2013, **88**, 144428.
55 Y. Liu, L. Yu, M. Sun, G. Diao, B. Lan and G. Cheng, *Comput. Theor. Chem.*, 2014, **1031**, 1–6.
56 F. Cheng, T. Zhang, Y. Zhang, J. Du, X. Han and J. Chen, *Angew. Chem., Int. Ed.*, 2013, **52**, 2474–2477.
57 H.-Y. Su, Y. Gorlin, I. C. Man, F. Calle-Vallejo, J. K. Norskov, T. F. Jaramillo and J. Rossmeisl, *Phys. Chem. Chem. Phys.*, 2012, **14**, 14010–14022.
58 C. R. A. Catlow, *Computer Modelling in Inorganic Crystallography*, Academic Press, San Diego, 1997.
59 J. R. Hill, C. M. Freeman and L. Subramanian, *Reviews in Computational Chemistry*, ed. K. B. Liphowitz and D. B. Boyd, Wiley, New York, 2000.
60 M. S. Islam and C. A. J. Fisher, *Chem. Soc. Rev.*, 2014, **43**, 185.
61 R. R. Maphanga, D. C. Sayle, T. X. T. Sayle and P. E. Ngoepe, *Phys. Chem. Chem. Phys.*, 2011, **13**, 1307.
62 R. R. Maphanga, S. C. Parker and P. E. Ngoepe, *Surf. Sci.*, 2009, **603**, 3184–3190.
63 T. X. T. Sayle, R. R. Maphanga, P. E. Ngoepe and D. C. Sayle, *J. Am. Chem. Soc.*, 2009, **131**, 6161.
64 T. X. T. Sayle, C. R. A. Catlow, R. R. Maphanga, P. E. Ngoepe and D. C. Sayle, *J. Am. Chem. Soc.*, 2005, **127**, 12828.
65 G. W. Watson, E. T. Kelsey, N. H. de Leeuw, D. J. Harris and S. C. Parker, *J. Chem. Soc., Faraday Trans.*, 1996, **92**, 433.
66 G. Kresse and J. Furthmüller, *Phys. Rev. B: Condens. Matter Mater. Phys.*, 1996, **54**, 11169–11186.
67 J. P. Perdew, K. Burke and M. Ernzerhof, *Phys. Rev. Lett.*, 1996, **77**, 3865.
68 M. Nolan, S. C. Parker and G. W. Watson, *Surf. Sci.*, 2005, **595**, 223–232.
69 B. J. Morgan and G. W. Watson, *J. Phys. Chem. C*, 2009, **113**, 7322.
70 G. K. H. Madsen and P. Novak, *Europhys. Lett.*, 2005, **69**, 777.
71 K. Schwarz and P. Blaha, *Comput. Mater. Sci.*, 2003, **28**, 259.
72 D. A. Tompsett, S. C. Parker, P. G. Bruce and M. S. Islam, *Chem. Mater.*, 2013, **25**, 536.
73 D. A. Tompsett, D. S. Middlemiss and M. S. Islam, *Phys. Rev. B: Condens. Matter Mater. Phys.*, 2012, **86**, 205126.
74 E. R. Ylvisaker, W. E. Pickett and K. Koepernik, *Phys. Rev. B: Condens. Matter Mater. Phys.*, 2009, **79**, 035103.
75 C. S. Johnson, D. W. Dees, M. F. Mansuetto, M. M. Thackeray, D. R. Vissers, D. Argyriou, C. K. Loong and L. Christensen, *J. Power Sources*, 1997, **68**, 570–577.
76 C. Franchini, R. Podloucky, J. Paier, M. Marsman and G. Kresse, *Phys. Rev. B: Condens. Matter Mater. Phys.*, 2007, **75**, 195128.
77 D. A. Tompsett, S. C. Parker and M. S. Islam, *J. Am. Chem. Soc.*, 2014, **136**, 1418.
78 S. Fritsch and A. Navrotsky, *J. Am. Chem. Soc.*, 1996, **79**, 1761.
79 X. Zhang, X. Sun, H. Zhang, D. Zhang and Y. Ma, *Electrochim. Acta*, 2013, **87**, 637–644.
80 Y. Chen, C. G. Liu, C. Liu, G. Q. Lu and H. M. Cheng, *Mater. Res. Bull.*, 2007, **42**, 1935–1941.
81 Y. Chen, C. Liu, F. Li and H.-M. Cheng, *J. Alloys Compd.*, 2005, **397**, 282–285.
82 X. Fu, J. Feng, H. Wang and K. M. Ng, *J. Solid State Chem.*, 2010, **183**, 883.
83 N. Tang, X. Tian, C. Yang, Z. Pi and Q. Han, *J. Phys. Chem. Solids*, 2010, **71**, 258.

84 G. A. E. Oxford and A. M. Chaka, *J. Phys. Chem. C*, 2011, **115**, 16992–17008.
85 D. Qian, Y. Hinuma, H. Chen, L.-S. Du, K. J. Carroll, G. Ceder, C. P. Grey and Y. S. Meng, *J. Am. Chem. Soc.*, 2012, **134**, 6096–6099.
86 V. Giordani, S. A. Freunberger, P. G. Bruce, J.-M. Tarascon and D. Larcher, *Electrochem. Solid-State Lett.*, 2010, **13**, A180–A183.
87 M. Sun, B. Lan, L. Yu, F. Ye, W. Song, J. He, G. Diao and Y. Zheng, *Mater. Lett.*, 2012, **86**, 18–20.
88 C. Stampfl, M. V. Ganduglia-Pirovano, K. Reuter and M. Scheffler, *Surf. Sci.*, 2002, **500**, 368–394.
89 D. M. Robinson, Y. B. Go, M. Mui, G. Gardner, Z. Zhang, D. Mastrogiovanni, E. Garfunkel, J. Li, M. Greenblatt and G. C. Dismukes, *J. Am. Chem. Soc.*, 2013, **135**, 3494–3501.